



Experimental determination of zirconium hydride precipitation and dissolution in zirconium alloy

E. Lacroix ^{a,*}, A.T. Motta ^a, J.D. Almer ^b

^a Department of Mechanical and Nuclear Engineering, The Pennsylvania State University, University Park, PA, 16802, USA

^b Advanced Photon Source, Argonne National Laboratory, Argonne, IL, 60439, USA

ARTICLE INFO

Article history:

Received 13 December 2017

Received in revised form

8 June 2018

Accepted 22 June 2018

Available online 23 June 2018

ABSTRACT

Synchrotron X-Ray transmission diffraction experiments were performed to study hydride precipitation and dissolution in the zirconium/zirconium-hydride system while it occurs. Evidence was found that the hysteresis between the terminal solid solubility for precipitation and dissolution is not observed when hydride particles are already present at the beginning of sample cooldown. Furthermore, experimental results show that, during a temperature hold, the concentration of hydrogen in solid solution becomes lower than the terminal solid solubility for hydride precipitation and eventually reaches the terminal solid solubility for hydride dissolution, indicating that the latter is the actual thermodynamic solubility limit.

© 2018 Published by Elsevier B.V.

1. Introduction

The ingress of hydrogen into nuclear fuel rod cladding during operation and the precipitation of brittle hydride particles can reduce cladding ductility [1,2]. Because of this, in addition to studying hydrogen pickup during corrosion, it is important to study the processes of hydrogen transport and hydride precipitation once the hydrogen enters the cladding. A model of hydrogen transport and hydride precipitation was proposed by Courty et al. [3], based on known processes of hydrogen mobility in the cladding, driven by both a concentration and a temperature gradient. The hydride precipitation and dissolution model in that study was based simply on the terminal solid solubilities for dissolution and precipitation [4] and on the kinetic model introduced by Marino [5]. The proposed model is summarized in Table 1.

In Table 1, C_{SS} is the hydrogen content in solid solution (in wt. ppm), C_P is the hydrogen in hydrides (in wt. ppm), TSS_P and TSS_D are the terminal solid solubilities for hydride precipitation and dissolution respectively (both expressed in wt. ppm), α^2 is the precipitation kinetics parameter, β^2 is the dissolution kinetics parameter (both in s^{-1}) and J is the hydrogen diffusion flux ($wt.ppm/cm^2/s$). While TSS_P , TSS_D and α^2 are determined experimentally, β^2 was assumed to be equal to 1 as hydride dissolution is fast [3]. α^2 was

measured experimentally by Kammenzind [6] and by Courty et al. in Ref. [7]. Since it was considered that a stress gradient was less influential than the other gradients, the hydrogen flux J , which leads to hydrogen redistribution, depends mainly on two physical phenomena: Fick's law of diffusion and thermodiffusion (the Soret effect).

$$J_{Diff} = -D\nabla C_{SS} - \frac{DQ^*C_{SS}}{RT^2}\nabla T \quad (1)$$

where D is the diffusion coefficient of hydrogen in Zircaloy (in m^2/s), Q^* the heat of transport (in J/mol), R the ideal gas constant (in J/mol/Kelvin) and T the temperature (in Kelvin). Although this model was implemented into the finite element code BISON and used to determine the hydrogen concentration in service, questions remain as to whether all the physics involved are properly considered.

The hydrogen solubility limits in precipitation and dissolution have been measured by several authors, who have in general reported a hysteresis between precipitation and dissolution [4,8–13]. However, previous results suggest that the hysteresis may not be present when hydrides are already precipitated at the start of cooldown [11]. Therefore, a better understanding of the hydride precipitation/dissolution hysteresis in this system is needed to understand these processes and to discern which of the two solubility limits is a true thermodynamic limit, rather than a kinetic effect. A series of experiments were therefore specifically designed to clarify these issues.

* Corresponding author.

E-mail address: eul152@psu.edu (E. Lacroix).

Table 1
Model for hydrogen precipitation and dissolution [3].

| Conditions | Model |
|---|---|
| if $C_{SS} > TSS_D$ and $C_P \geq 0$ | $\begin{cases} \frac{dC_P}{dt} = \alpha^2(C_{SS} - TSS_P) \\ \frac{dC_{SS}}{dt} = -\nabla J - \alpha^2(C_{SS} - TSS_P) \end{cases}$ |
| if $C_{SS} < TSS_D$ and $C_P > 0$ | $\begin{cases} \frac{dC_P}{dt} = -\beta^2(TSS_D - C_{SS}) \\ \frac{dC_{SS}}{dt} = -\nabla J + \beta^2(TSS_D - C_{SS}) \end{cases}$ |
| if $C_{SS} < TSS_D$ and $C_P = 0$ or if $TSS_D \leq C_{SS} < TSS_P$ and $C_P \geq 0$ | $\begin{cases} \frac{dC_P}{dt} = 0 \\ \frac{dC_{SS}}{dt} = -\nabla J \end{cases}$ |

2. Experimental methods

The material used for this experiment was cold-worked stress-relieved (CWSR) Zircaloy-4 sheet provided by ATI Specialty Alloys and Components. The material texture was such that the basal poles were inclined approximately $\pm 30^\circ$ away from the normal direction of the sheet [14,15]. The Kearns factors [16] were measured to be $f_N = 0.59$, $f_L = 0.05$ and $f_T = 0.31$ in the normal, longitudinal and transverse directions respectively. These values are similar to those normally obtained in CWSR Zircaloy-4 cladding [17].

The material was hydrided using gaseous charging in an atmosphere of 1% hydrogen and 99% argon. Prior to gaseous charging, samples were etched with a solution of 10% Hydrofluoric Acid (49% concentrated), 45% Nitric Acid (79% concentrated) and 45% deionized water to remove the native oxide layer. A 20 nm layer of Nickel was then sputtered onto the etched surface to protect it against air corrosion, using a Kurt J. Lesker CMS (Combinatorial Material Science) series sputter machine. Hydriding by gaseous charging was performed by first creating a secondary vacuum ($\sim 10^{-6}$ Torr) and then introducing the desired amount of hydrogen into the loading chamber. The loading chamber was heated to 450°C to allow hydrogen absorption and diffusion while ensuring that the absorbed hydrogen remain in solid solution. Once the target temperature and vacuum was reached, the control volume valve was opened and hydrogen was released into the loading chamber. The system remained as such for 2 h to allow hydrogen to be absorbed and to diffuse into the material. The hydrogen content in the sample studied after gas charging was measured to be 255 ± 43 wt. ppm by Luvak Inc., using Vacuum Hot Extraction (in accordance with ASTM E146). The hydrided sheet was then machined into a uniaxial testing dog-bone configuration using wire electrical discharge machining. The sample geometry is shown in Fig. 1a. This sample was examined at the 1-ID-E beamline at the Advanced Photon

Source at Argonne National Laboratory using an 80.725 keV X-ray beam capable of completely penetrating through a 0.6 mm thick sample. The beam size was $100 \times 100 \mu\text{m}$. The diffraction patterns generated were recorded using a GE 41RT area detector, while the sample was heated and cooled in a furnace, as shown schematically in Fig. 1b.

The diffraction pattern showed peaks that could be indexed as coming from both the Zr matrix and the hydride phase. As in other studies we performed, only peaks associated with the delta hydride phase were observed – no peaks from other hydride phases such as γ , ϵ or ζ were observed. The intensity of the $\delta(111)$ hydride diffraction peak was used as a gauge of the hydride volume fraction in the sample. Accordingly, the evolution of the $\delta(111)$ hydride peak integrated intensity with respect to time and temperature was determined by recording a diffraction pattern every 16 s and determining the integrated intensity under the peak. The diffraction patterns were obtained by summing over 18 diffraction patterns taken for 0.5 s each. The time per pattern was chosen to avoid detector saturation from the strongest zirconium peaks, and the summation provided sufficient signal-to-noise ratio for the hydride peaks. The $\delta(111)$ hydride peak intensity was obtained by integrating along the full diffraction ring. Because the $\delta(111)$ hydride peak is located at the tail of the stronger $(10\bar{1}0)$ Zr peak, it was necessary to fit these together as a pair of Pseudo Voigt functions.

The integrated peak intensity of the $\delta(111)$ hydride at each time step of this heat treatment was one of the parameters extracted from the pseudo-voigt fits. The integrated $\delta(111)$ hydride diffracted intensity is related to the hydrogen content in solid solution by:

$$C_{SS}(t) = C_{VHE} \left(1 - \frac{I(t)}{I_m} \right) \quad (2)$$

where $C_{SS}(t)$ is the hydrogen content in solid solution at time t , C_{VHE} is the total hydrogen content measured using Vacuum Hot Extraction, $I(t)$ is the integrated intensity of the $\delta(111)$ hydride peak at time t and I_m is the intensity of the $\delta(111)$ hydride diffraction peak when the hydrides are fully precipitated. Equation (2) assumes that the hydride texture does not vary significantly during precipitation and dissolution so that the $\delta(111)$ hydride peak is a valid measure of the hydride volume fraction. This assumption was partly verified during the experiment. The (111) δ -hydride peak intensity was measured as a function of the chi angle of the diffraction ring at the beginning and the end of the experiment and no significant difference was observed, suggesting that the texture remained the same during the experiments. Also the integration of the diffracted intensity over the chi angle showed a constant value during the experiment, suggesting that little hydrogen was lost from the sample.

The type K thermocouple used by design yields a measurement error corresponding to the largest of 2.2°C or 0.75% of the recorded

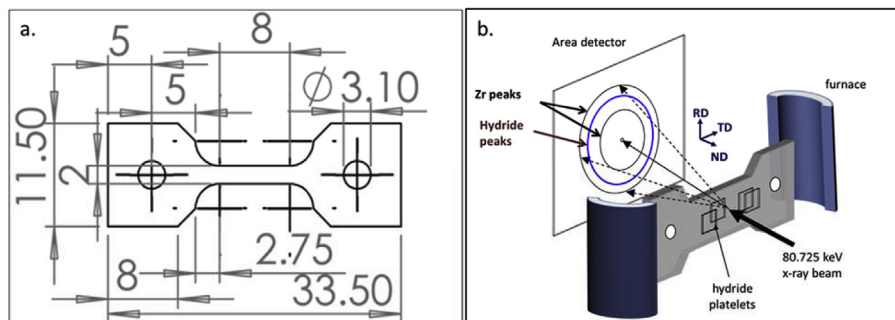


Fig. 1. (a) Dog-bone tensile testing sample dimensions (dimensions in mm), (b) Schematic depiction of the experimental setup at APS after [7].

value. The errors coming from the hydrogen content itself were calculated to be from both the fit and the statistical error. Assuming the events from the photon source follow a Gaussian distribution, the statistical error is defined by \sqrt{N} . The fitting error was assessed by running diffraction patterns of different intensities 500 times during one heat-up cycle, giving an error as a function of intensity. Three standard deviation in the measurements did not exceed 2.53% of the average intensity measured and so the fitting error was assumed to be 2.6% in Fig. 3.

3. Experimental results

The temperature history imposed on the sample during the experiment is shown in Fig. 2. As the sample temperature was increased or decreased, the hydrides dissolved and precipitated, while the diffraction intensity was measured as described above. The integrated intensity of the $\delta(111)$ hydride peak was used to calculate the hydrogen concentration in solid solution using equation (2). The evolution of the hydrogen content in solid solution is plotted versus temperature in Fig. 3 and discussed in the following. Each cycle is now discussed in detail:

First cycle (green lozenges in Fig. 3): Hydride precipitation after complete dissolution at high temperature.

Starting at room temperature, the sample was gradually heated at a rate of 10 °C/min to 425 °C (point 1), and held at temperature for 10 min. This temperature is high enough to dissolve all the hydrides present in the sample; this was in fact verified by the $\delta(111)$ hydride diffraction peak intensity reaching the same intensity as the background at the maximum temperature, meaning that the concentration of hydrogen in solid solution C_{SS} is 255 wt. ppm. The sample was then cooled at a rate of 10 °C/min to 170 °C (point 2). As the sample is cooled, precipitation only starts when the sample reaches the TSS_D curve at ~355 °C (point 1'). From then on, the hydrogen content in solid solution decreases as hydride particles precipitate and grow, following the TSS_D curve, until the target temperature 170 °C is reached (point 2), at which point almost all hydrogen in the sample is precipitated into hydrides. Fig. 3 shows that during continuous heating and cooling, the calculated hydrogen content in solid solution roughly follows the TSS_D and TSS_P solubility limits respectively with a hysteresis, as normally reported in the literature [4,8–13].

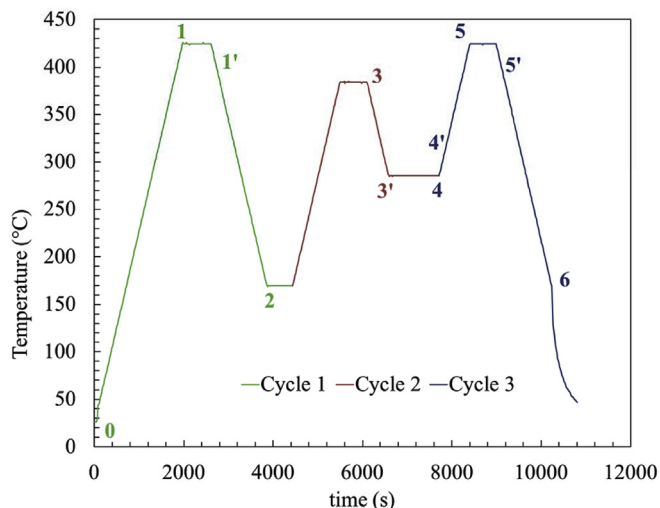


Fig. 2. Heat treatment applied to the studied sample.

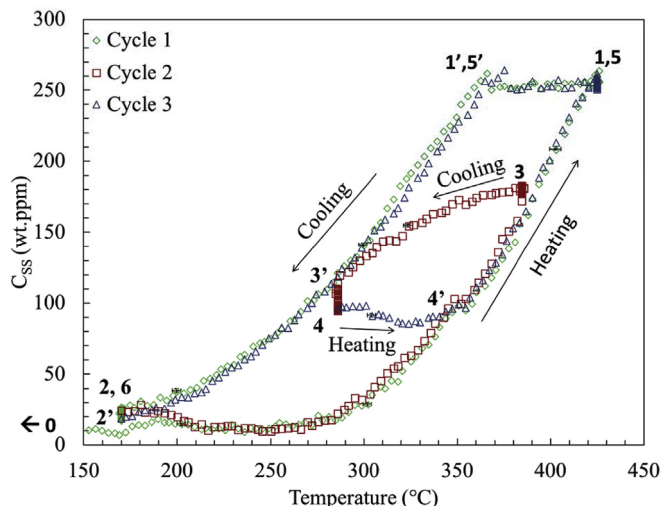


Fig. 3. Hydrogen Concentration in solid solution calculated using equation (2) as a function of temperature, for a sample containing 255 wt. ppm of hydrogen, undergoing the heat treatment represented in Fig. 2.

Second cycle (red squares): Hydride precipitation with incomplete hydride dissolution.

After a hold time of 20 min at 170 °C, the sample was then heated to 385 °C at a rate of 10 °C/min (point 3). At this temperature not all hydrides are dissolved: about 75 wt. ppm. of hydrogen is stable as zirconium hydrides. The sample was then cooled at the same rate as in the previous cycle (10 °C/min) to 285 °C (point 3'). As the sample temperature decreases from 385 to 285 °C, the amount of hydrogen in solid solution *immediately* starts to decrease, indicating that when hydrides are present, precipitation of additional hydrogen occurs without hysteresis. The sample was then held at 285 °C (between 3' and 4) for 20 min. Interestingly, further hydride precipitation occurred during this latter temperature hold, as shown by the decrease in the amount of hydrogen in solid solution. The conclusion of this cycle is that the hysteresis is due to hydride nucleation, as further discussed below.

Third Cycle (blue triangles): Dissolution after hydride precipitation.

After a hold time of 20 min at 285 °C, the temperature was again increased to 425 °C at 10 °C/min, to dissolve all the hydrides (step 4 to 4' to 5). It is also interesting to note that despite the temperature being increased, a slight *decrease* in hydrogen content in solid solution initially occurred during that experiment – the C_{SS} going from ~96 wt. ppm at point 4 (285 °C) to ~86 wt. ppm half way towards point 4' (306 °C) – thus suggesting that hydrogen continued to precipitate in the hysteresis region *as long as the hydrogen in solid solution was greater than TSS_D* . It is only when the temperature approaches the TSS_D curve that hydrogen dissolution is again observed. The sample was then cooled down to 170 °C at 10 °C/min (step 6), and air cooled to room temperature.

The drop in C_{SS} observed between 3' and 4 in Fig. 3 can be clearly discerned in Fig. 4. These results show that hydrogen precipitates into hydrides even when C_{SS} is lower than TSS_P , suggesting that TSS_P is a *kinetic* parameter, rather than a thermodynamic equilibrium solubility.

Between point 4 and 4' the hydrogen content in solid solution initially decreases with increasing temperature. This is likely because, as the temperature rises, the hydrogen mobility increases, and because the sample is still in the hysteresis region, additional

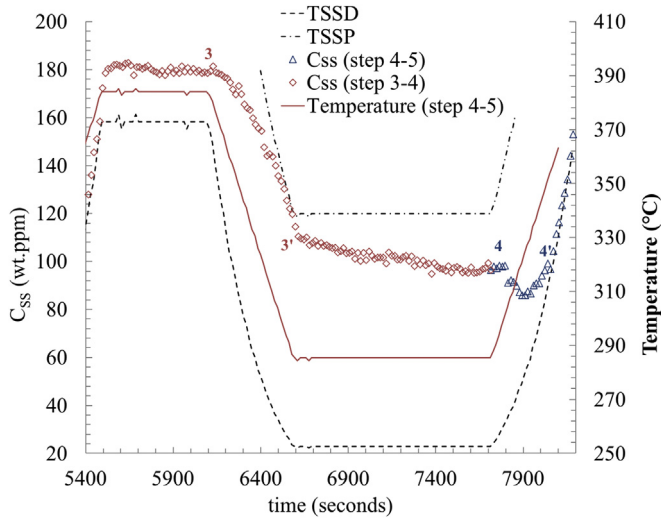


Fig. 4. Temporal evolution of steps 3 through 4', showing hydride growth between TSSP and TSSD.

precipitation can occur. Eventually the sample reaches the TSS_D and the hydrogen in solid solution starts to increase again as the hydrides dissolve. This suggests that the offset between this point and the curve labelled TSS_D in Fig. 4 is caused by dissolution kinetics and that precipitation continues to happen until TSS_D is reached. The TSS_D and TSS_P curves plotted here are interpolations of the paths 0–1 and 1'–2 respectively followed in cycle 1, to allow the comparison of the behavior of the hydrogen in solid solution in the path 3–4' to the hydrogen behavior in the previous cycle. Point 3 is located slightly above the curve followed in continuous heating (path 0–1, 2'–5). While more data would be needed to prove consistency in the behavior and support this statement, it appears that hydride dissolution is not instantaneous and can be detected from the decrease in the diffracted hydride intensity as it develops while the temperature is held at 385°C for 10 minutes.

4. Discussion

The kinetics of hydride precipitation were modeled by Marino as:

$$\frac{dC_P}{dt} = \alpha^2 (C_{SS} - C_{eq}) \quad (3)$$

where C_P is the hydrogen content in hydride form, C_{eq} is the amount of hydrogen in solid solution in the matrix in equilibrium with the hydrides, C_{SS} the amount of hydrogen in solid solution and α^2 is a kinetics parameter [6].

In previous models ([3,18]) C_{eq} was taken to be equal to TSS_P, which assumes that TSS_P is a thermodynamic solubility limit. The results shown in Figs. 3 and 4 indicate this is not the case, which makes those analyses questionable. However the results can be reconciled with Marino's model [5] if one takes $C_{eq} = TSS_D$ in equation (3).

To verify that hydride precipitation can occur when the hydrogen concentration in solid solution lies between the two TSS curves, we have reanalyzed the data from the experiments conducted in Ref. [7]. These experiments were designed to measure the kinetic parameter α^2 in equation (2) [5]. In the experiment the samples used were cold-worked stress-relieved Zircaloy-4 sheet machined into test coupons of dimensions 1 cm × 4.2 cm and 660 μm thick which were recrystallized at 640 °C for 7 min and

then hydrided in the same manner as described in section 2, in this case to a hydrogen content of 541 wt. ppm. The resulting hydrided sample was heated to a high enough temperature (535 °C) to dissolve all hydrides and then cooled as fast as possible (about 2 °C/s) to various target temperatures between 280 and 400 °C, thus creating a hydrogen supersaturation in solid solution. If it is assumed that the hydrogen precipitation follows equation (3), the fitting of the evolution of the hydride diffraction peak during a hold time at the target temperature for several hours allows the measurement of the α^2 kinetic parameter. In the initial analysis, following Kammenzind [6] it was assumed $C_{eq} = TSS_P$.

These experiments were re-analyzed for the purpose of this study, but this time by assuming that $C_{eq} = TSS_D$. Fig. 5 shows a single experiment performed in Ref. [7]. The sample was first heated to a dissolution temperature (535 °C) at which the $\delta(111)$ hydride peak could not be observed, indicating total hydride dissolution in the sample. The sample was then cooled down to the target temperature of 380 °C at a rate of approximately 2 °C/s (pt. 1 in Fig. 5). During cooldown, the hydrogen remained in solid solution until hydrides could nucleate so that precipitation could start (pt. 2). Throughout the cooling process, the sample followed the TSS_P curve, as expected, until the target temperature of 380 °C was reached (pt. 3). A slight oscillation between 379 °C and 381 °C can be observed, which can be due to the error in thermocouple measurement (± 2.85 °C), or a delay in control in the temperature controller. Fig. 6 shows the concentration of hydrogen in solid solution C_{SS} , calculated using equation (2) for similar experiments conducted at the various target temperatures.

Fig. 6 shows six different runs to the target temperatures indicated in the legend from Ref. [7], for a sample containing 541 wt. ppm. Note that at the fast heating rate used, hydride dissolution during heating is not in equilibrium, as shown in Fig. 6: the hydrogen dissolution curve is considerably below the TSS_D curve, indicating that dissolution does not occur instantaneously. The temperature was then held at 535 °C for 30 min to ensure that the hydrides were fully dissolved, and then lowered to several target temperatures (288, 316, 332, 360, 380 and 400 °C) at 2 °C/s and held at the target temperature for 2 h. It is clear that in each case the C_{SS} falls far below the TSS_P showing that hydride precipitation occurs until TSS_D. The concentration of hydrogen in solid solution C_{SS} continues to decrease even when the concentration of hydrogen in solid solution falls below TSS_P indicating hydride precipitation in the hysteresis region. In fact, as time progresses, the

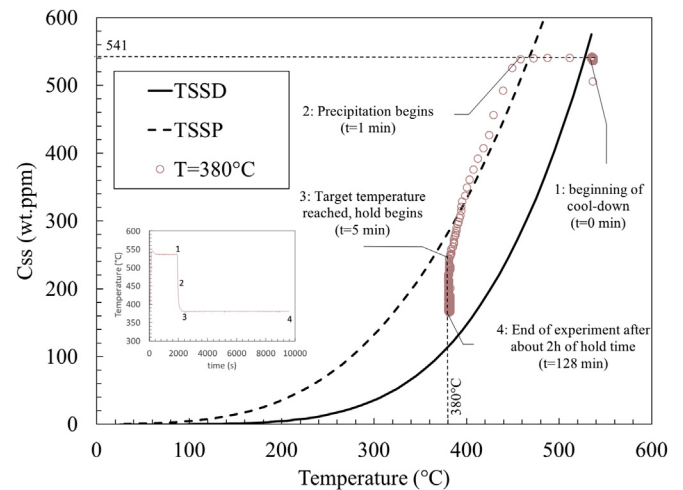


Fig. 5. Analysis of Courty's experimental data [7], results compared to literature data for TSS_P and TSS_D from Zanellato [10].

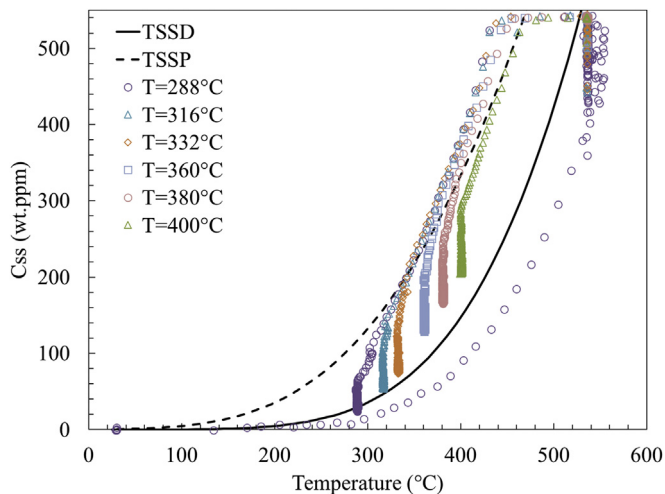


Fig. 6. The concentration of hydrogen in solid solution during long hold times at the target temperatures indicated, in a sample containing 541 wt. ppm of hydrogen, compared to literature values of TSS_P and TSS_D [10].

C_{SS} becomes closer and closer to TSS_D . This shows that hydrides precipitate continuously throughout the experiment, thus confirming that hydrides can precipitate in the region between TSS_P and TSS_D if hydride particles are already present in the matrix. This is in agreement with the data shown in Fig. 4 where hydrogen continued to precipitate until the TSS_D was reached. This further suggests that TSS_D is the equilibrium solubility.

This study indicates that the commonly observed hysteresis in the Zr/ZrH_x system is due to the additional energy needed for hydride nucleation [3,9,10,12]. This study also agrees with previous observations from Colas, who showed that hydrogen can precipitate while in the hysteresis region if hydrides are already present (i.e. if hydride nucleation is not needed) [11]. It was observed in this study that not only do previously nucleated hydrides allow precipitation between TSS_D and TSS_P but that a hold at temperature means that hydride precipitation will continue until the hydrogen concentration in solid solution reaches TSS_D . This result suggests that hydride nucleation is the principal reason for the apparent hysteresis observed in the Zr/ZrH_x system.

This understanding of the hysteresis may help understand further the differences in the measurements performed in materials that are recrystallized, mechanically loaded or irradiated. A difference in TSS_P should be expected if any change in nucleation-inducing factors is made to the material. Therefore, recrystallized and irradiated materials may have a change in hysteresis behavior from a change in the respective densities of hydride nucleation site, such as grain boundaries. However, hydrogen trapping in grain boundaries or dislocations [4,13] has been shown to be of importance as well in the measured value of TSS_P and could be a competing effect to the nucleation site addition with additional grain boundaries or dislocations, since grain boundaries and dislocations can act both as hydrogen traps and as nucleation sites. The effect of applied stress on the TSS_P should be assessed more carefully in future studies.

5. Conclusions

Synchrotron X-ray diffraction experiments were performed in order to observe hydrogen precipitation in the hysteresis region. These experiments confirmed that hydrogen can precipitate into zirconium hydrides without any hysteresis if hydrides are already present in the system at the start of cooldown. The experimental

results obtained in Ref. [7] were re-analyzed and the results confirmed results showed in Fig. 4 that TSS_P is not an equilibrium solubility limit but, rather, corresponds to the maximum amount of hydrogen supersaturation that the zirconium matrix can accommodate at a given temperature before nucleation of new hydride particles starts. Once that supersolubility limit is reached, hydrogen starts precipitating into hydrides and continues to precipitate until the hydrogen content in solid solution reaches the TSS_D , bringing the system back to its equilibrium state. This result implies that:

- The hydride nucleation barrier is the main reason the precipitation/dissolution hysteresis exists in the Zr/ZrH_x system.
- Previous models of hydrogen precipitation need to be revised to take into account the equilibrium value of hydrogen in solid solution which in turn will allow for a reliable measurement of the precipitation kinetics.

This study showed evidence that the effects of dissolution kinetics are visible at heating rates used in the experiments performed and presented in this study (10°C/min and 2°C/min). Evidence was also shown that hydrogen mobility is contributing to the temperature dependence of the precipitation kinetics, which is initially stronger than the effect of the driving force.

Acknowledgement

This research was funded by DOE NEUP project 13–5180 of the US Department of Energy. We also thank Peter Kenesei, Jun-Sang Park and Pierre-Clément Simon for their help in performing the experiment. We thank the Penn State Nanofab staff for their assistance in the preparation of the samples. Use of the Advanced Photon Source was supported by the U.S. Department of Energy, Office of Basic Energy Sciences under Contract No. DE-AC02-06CH11357.

References

- [1] G. Bertolino, G. Meyer, J.P. Ipina, Degradation of the mechanical properties of Zircaloy-4 due to hydrogen embrittlement, *J. Alloy. Comp.* 330–332 (2002) 408–413.
- [2] J. Desquines, D.A. Koss, A.T. Motta, B. Cazalis, M. Petit, The issue of stress state during mechanical tests to assess cladding performance during a reactivity-initiated accident (RIA), *J. Nucl. Mater.* 412 (2011) 250–267.
- [3] O. Courty, A.T. Motta, J.D. Hales, Modeling and simulation of hydrogen behavior in Zircaloy-4 fuel cladding, *J. Nucl. Mater.* 452 (2014) 311–329.
- [4] A. McMinn, E.C. Darby, J. Schofield, The terminal solid solubility of hydrogen in zirconium alloys, in: *Zirconium in the Nuclear Industry: Twelfth International Symposium*, 2016, pp. 173–195. ASTM STP 1354.
- [5] G.P. Marino, Hydrogen supercharging in zircaloy, *Mater. Sci. Eng.* 7 (6) (1971) 335–341.
- [6] B. Kammenzind, D. Franklin, H. Peters, W. Duffin, Hydrogen pickup and redistribution in alpha-annealed Zircaloy-4, in: *Zirconium in the Nuclear Industry: Eleventh International Symposium*, 1996, pp. 338–370. ASTM STP 1295.
- [7] O. Courty, A.T. Motta, C.J. Piotrowski, J.D. Almer, Hydride precipitation kinetics in zircaloy-4 studied using synchrotron X-ray diffraction, *J. Nucl. Mater.* 461 (2015) 180–185.
- [8] J.J. Kearns, Terminal solubility and partitioning of hydrogen in the alpha phase of zirconium, Zircaloy-2 and Zircaloy-4, *J. Nucl. Mater.* 22 (1967) 292–303.
- [9] K. Une, S. Ishimoto, Dissolution and precipitation behavior of hydrides in Zircaloy-2 and high Fe Zircaloy, *J. Nucl. Mater.* 322 (2003) 66–72.
- [10] O. Zanellato, M. Preuss, J.Y. Buffiere, F. Ribeiro, A. Steuwer, J. Desquines, J. Andrieux, B. Krebs, Synchrotron diffraction study of dissolution and precipitation kinetics of hydrides in Zircaloy-4, *J. Nucl. Mater.* 420 (2012) 537–547.
- [11] K. Colas, A.T. Motta, M.R. Daymond, J. Almer, Mechanisms of hydride reorientation in Zircaloy-4 studied in situ, in: *Zirconium in the Nuclear Industry: 17th International Symposium*, 2014, pp. 1107–1137. ASTM STP 1543.
- [12] Z.L. Pan, I.G. Ritchie, M.P. Puls, The terminal solid solubility of hydrogen and deuterium in Zr-2.5Nb alloys, *J. Nucl. Mater.* 228 (1996) 227–237.
- [13] P. Vizcaino, A.D. Banchik, J.P. Abriata, Solubility of hydrogen in Zircaloy-4: irradiation induced increase and thermal recovery, *J. Nucl. Mater.* 304 (2002) 96–106.

- [14] P. Raynaud, D.A. Koss, A.T. Motta, K.S. Chan, Fracture toughness of hydrided Zircaloy-4 sheet under through-thickness crack growth conditions, in: *Zirconium in the Nuclear Industry: 15th International Symposium, 2007*, pp. 163–177. ASTM STP 1505.
- [15] E. Tenckhoff, Review of deformation mechanisms, texture and mechanical anisotropy in zirconium and zirconium base alloys, in: *Zirconium in the Nuclear Industry: 14th International Symposium, 2005*, pp. 1–26. ASTM STP 1467.
- [16] J.J. Kearns, C.R. Woods, Effect of texture, grain size and cold work on the precipitation of oriented hydrides in Zircaloy tubing and plate, *J. Nucl. Mater.* 20 (1966) 241–261.
- [17] P. Delobelle, et al., A unified model to describe the anisotropic viscoplastic Zircaloy-4 cladding tubes, in: *Zirconium in the Nuclear Industry: 11th International Symposium, 1996*, pp. 373–393. ASTM STP 1295.
- [18] D.S. Stafford, Multidimensional simulations of hydrides during fuel rod life-cycle, *J. Nucl. Mater.* 466 (2015) 362–372.